Boron Nitride Nanosheet Coatings with Controllable Water Repellency

Amir Pakdel,[†,‡,*] Chunyi Zhi,[‡,*] Yoshio Bando,[‡] Tomonobu Nakayama,[†,‡] and Dmitri Golberg[†,‡,*]

[†]Graduate School of Pure and Applied Sciences, University of Tsukuba, Tennodai 1, Tsukuba, Ibaraki 305-0005, Japan, and [‡]International Center for Materials Nanoarchitectonics (MANA), National Institute for Materials Science (NIMS), Namiki 1-1, Tsukuba, Ibaraki 305-0044, Japan

ABSTRACT The growth, structure, and properties of two-dimensional boron nitride (BN) nanostructures synthesized by a thermal chemical vapor deposition method have been systematically investigated. Most of the BN nanosheets (BNNSs) were less than 5 nm in thickness, and their purity was confirmed by X-ray energy dispersive spectroscopy, X-ray photoelectron spectroscopy, electron energy loss spectroscopy, and Raman spectroscopy. The effects of the process variables on the morphology and roughness of the coatings were studied using atomic force microscopy and scanning electron microscopy. A smooth BN coating was obtained at 900 °C, while compact BNNS coatings composed of partially vertically aligned nanosheets could be achieved at 1000 °C and higher temperatures. These nanosheets were mostly separated and exhibited high surface area especially at higher synthesis temperatures. The nonwetting properties of the BNNS coatings were independent of the water pH and were examined by contact angle goniometry. The present results enable a convenient growth of pure BNNS coatings with controllable levels of water repellency, ranging from partial hydrophilicity to superhydrophobicity with contact angles exceeding 150°.

KEYWORDS: boron nitride nanosheets · chemical vapor deposition · Raman spectroscopy · surface morphology · atomic force microscopy · superhydrophobicity

Recent research progress on single-layer graphene and multilayer carbon nanosheets with thicknesses below 20 nm illuminated the importance of two-dimensional (2D) nanostructures on account of their extraordinary properties such as high surface-to-volume ratio, superior strength, sharp open edges, and eminent room-temperature carrier mobility.[1−4] These 2D nanomaterials have attracted a great deal of attention academically and also promise numerous applications in biosensing, hydrogen storage, ultracapacitors, composite filling, gas detection, and electron emission.[2−9] The structural similarity of carbon (C) and boron nitride (BN) nanomaterials created a lot of curiosity about the latter ones. Layered BN is an analogue of graphite in which alternating boron (B) and nitrogen (N) atoms substitute for C atoms in a honeycomb network with sp^2 bonding. Within each layer of hexagonal BN (h-BN), B and N atoms are bound by covalent bonds, whereas the layers are held together by van der Waals forces.[9] A 2D BN crystal structure can exhibit unique features such as superb thermal conductivity, excellent mechanical strength, remarkable chemical stability, magnetism, and electrical conductivity.[10,11] 2D BN nanostructures have been prepared by several methods, including decomposition of borazine, ultrasonication processing of h-BN, peeling by Scotch adhesive tapes, and chemical exfoliations of h-BN in ways similar to graphene fabrication.[10−12] Also, in order to take advantage of the aforementioned properties of BN, different methods have been proposed for preparing BN coatings on carbon nanotubes (CNTs)[13−15] and on other types of inorganic fibers,[16,17] which would be of great value for the design of nanoscale electronic devices and nanostructured composites.[18]

Nanostructured films of BN have shown superb hydrophobicity, although BN coatings without nanostructure features are hydrophilic surfaces.[19] In general, wettability of a surface depends on its chemical composition and microstructural geometry.[20] Nonwetting surfaces with high water contact angles (CA) can be prepared *via* two approaches: chemical functionalization of the surface with materials of low surface free energy[21] and creating micro/nanoscale roughness on the surface.[20] Superhydrophobicity is achieved if the CA of water on a surface reaches 150°. So far, many superhydrophobic coatings have been made of organic materials with low surface free energies, such as silicon-based hydrocarbons,[22,23] fluorohydrocarbons,[24] and fluorinated polymers.[25] Also, several works on the preparation of rough structures have been carried out, such as making electrodeposited gold cluster films,[26] anodic oxidation of aluminum,[27] fabricating densely packed aligned CNTs,[28] films of zinc oxide (ZnO)[29] and titanium oxide (TiO_2) nanowires,[30,31] hierarchical self-assemblies of 4,5-diphenylimidazole on copper,[32] Si pyramid/nanowire binary structures,[33] and nanosphere lithography.[34] However, most of these materials are not applicable at high temperatures and harsh

* Address correspondence to PAKDEL.Amir@nims.go.jp, ZHI.Chunyi@nims.go.jp, GOLBERG.Dmitri@nims.go.jp.

Received for review May 19, 2011 and accepted July 18, 2011.

Published online July 18, 2011
10.1021/nn201838w

environments. Highly hydrophobic coatings possess significant advantages such as water repelling, antifouling, and self-cleaning properties,[35] which appoint them an important role in anticorrosion, resisting water coalescence, and fog condensation systems.[35−37] Moreover, the hydrophobic coatings offer further promise for the formation of high-performance nanostructured surfaces with multifunctionality that can be used in optical, photoelectric, microelectronic, catalytic, and biomedical applications.[38−42] Undoubtedly, the ability to produce hydrophobic films of diminutive structures such as BN nanosheets (BNNSs) is beneficial for many branches of modern science and technology.

Here we report a simple and efficient approach for the direct fabrication of BNNSs on silicon/ silicon dioxide (Si/SiO_2) substrates by thermal chemical vapor deposition (CVD) in a conventional horizontal tube furnace using B, magnesium oxide (MgO), and iron oxide (FeO) powders as precursors and ammonia (NH_3) gas flow. The systematic procedure for controlling the size, shape, and wettability of BNNSs was established. A similar growth system has been used recently for the synthesis of BN nanotubes (BNNTs);[43] thus we believe this approach can pave the way for enhancing the research activity in regard to BN nanostructures and their smart integration into modern technologies.

RESULTS AND DISCUSSION

Figure 1 depicts a schematic illustration of the synthesis conditions of the BNNSs. The Si/SiO_2 substrate on top of the combustion boat and the closed-end quartz test tube help to trap and accumulate the growth vapors,[43] which reacted with the NH_3 gas entering the boat and formed BNNSs on the substrate.

Figure 2 shows the scanning electron microscope (SEM) images of the samples grown for 30 and 60 min at the synthesis temperatures of 900, 1000, 1100, and 1200 °C. The morphology of the as-grown coating was found to be strongly dependent on the process variables, *i.e.*, growth time and temperature. A very fine BN coating was obtained at 900 °C (Figure 2a); however, partially vertical nanosheets could be achieved at 1000 °C (Figure 2b) and higher temperatures (Figure 2c, d). The coatings exhibit high surface area, especially at higher synthesis temperatures, and are composed of compact nanosheets that are mostly separated and partially aligned, although no electric field or templates were used.

SEM images in Figure 2 indicate that BNNSs display a uniform size distribution. Moreover, by increasing the growth time and/or the growth temperature, larger-sized nanosheets were formed and the relative spacing between the vertical BNNSs increased. Evidently the growth rate of the BNNSs was faster at higher temperatures, comparable to the growth rate reported for carbon nanosheets.[44,45] The nanosheet deposition on the substrate can be explained by the theory of

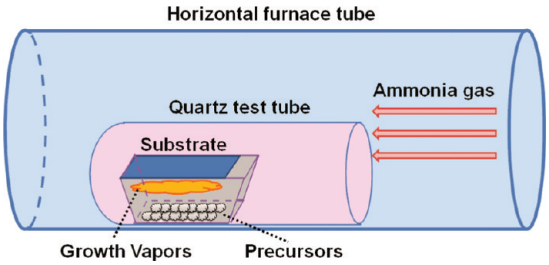

Figure 1. Schematic illustration of the apparatus used for the synthesis of the BNNS coatings.

nucleation[46,47] and the subsequent growth of the BNNSs. In fact, the accumulation of the trapped growth vapors due to the synthesis conditions (shown in Figure 1) would increase the reactive B_xO_y vapor pressure, leading to an enhancement of the probability of nucleation of the BNNSs.

Comparing parts b and f of Figure 2, we suggest that before the onset of the vertical growth of the BNNSs, there was a planar growth stage, in which the base layers were flat and parallel to the substrate. After the development of sufficient levels of force at grain boundaries, the leading edges of the top layers curled upward and the vertical growth of the nanosheets began. BN species at the synthesis temperature (≥1000 °C) could be assumed to have very high mobility; therefore, upon landing on the surface of a growing BNNS, they quickly moved along the surface toward the edge of the nanosheet and covalently bonded to the edge atoms before being re-evaporated. Thus, the BNNSs tended to grow higher rather than thicker. BN species diffusing toward the substrate instead of toward the growing edges could be re-evaporated due to the weak van der Waals forces connecting them to the substrate. That is why partially vertically aligned BNNSs rather than thick layers of BN oriented parallel to the substrate grew on the Si/SiO_2 wafers, as seen in Figure 2b, c, and d. A similar mechanism has been proposed for the formation of vertically standing carbon nanosheets (CNSs) produced by radio frequency plasma enhanced CVD, where the existence of an electric field promotes the growth of the CNSs perpendicular to the substrate.[45]

The BNNSs were characterized by transmission electron microscopy (TEM), as shown in Figure 3. The low-magnification TEM image in Figure 3a reveals the transparency of the nanosheets synthesized at 1200 °C to the electron beam due to their very small thicknesses. Also, as an intrinsic property for 2D nanostructures, bending and scrolling of the nanosheets can be noticed in Figure 3a similar to those reported for BNNSs prepared by other methods.[11,48,49] The inset of Figure 3a shows the selected area electron diffraction (SAED) pattern of region A, indicating the distinctive hexagonal structure of h-BN films.[50] High-resolution TEM (HRTEM) images of regions B, C, and D of Figure 3a

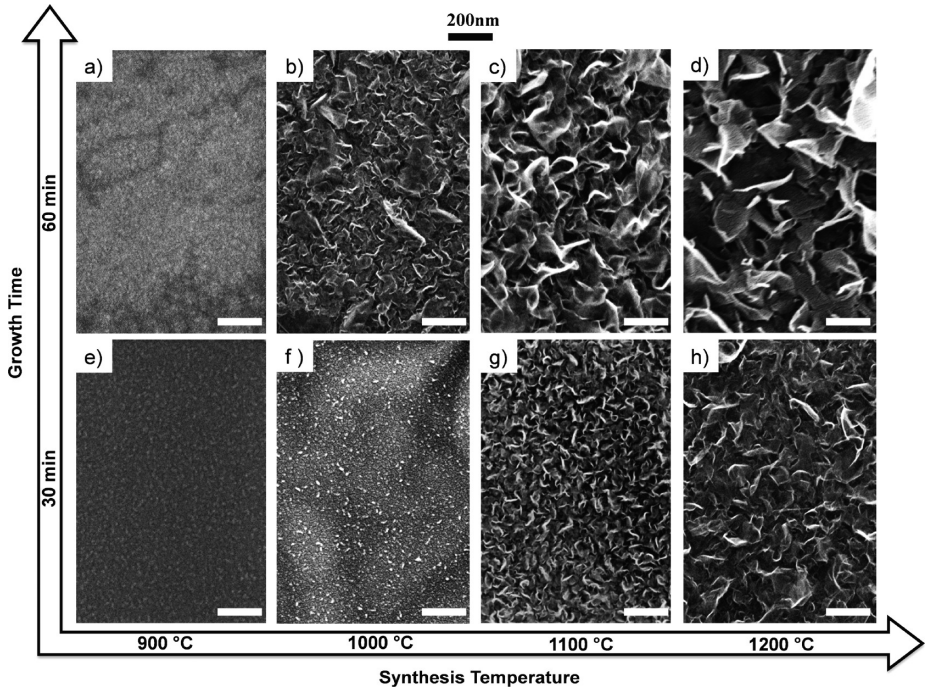

Figure 2. SEM images of the coatings synthesized at 900−1200 °C for 30 and 60 min.

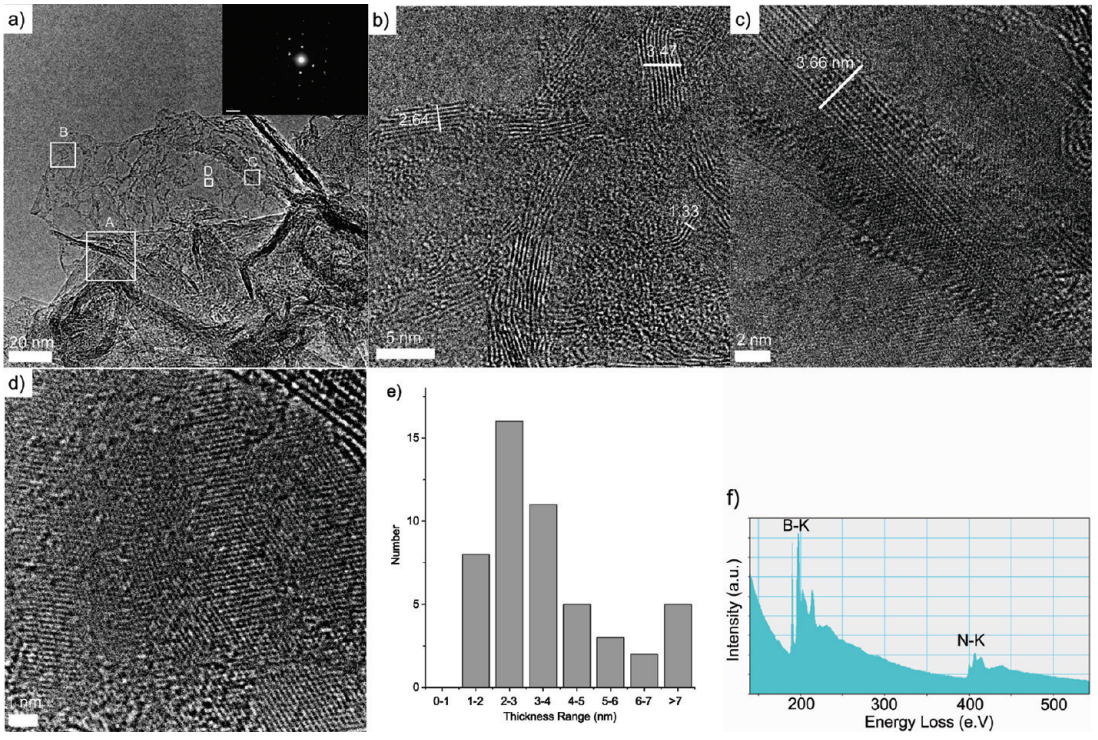

Figure 3. (a) Low-magnification TEM image of the BNNSs synthesized at 1200 °C for 30 min. (b, c, d) HRTEM images of the areas marked in panel (a) as B, C, and D, respectively. (e) Statistics of the thickness distribution of BNNSs. (f) Typical EEL spectrum of the BNNSs.

are shown in Figure 3b, c, and d, respectively. Highly ordered lattice fringes can be observed in Figure 3b and c, indicating that the BNNSs are well-crystallized. Measurements on many nanosheets revealed the spacing between adjacent fringes to be in the range 0.333− 0.351 nm. The average spacing is deduced to be 0.343 nm, quite close to the (002) interplanar distance in layered BN materials. Curled edges of nanosheets in Figure 3b and c made it possible to evaluate the sheet thicknesses. Statistics of the sheet

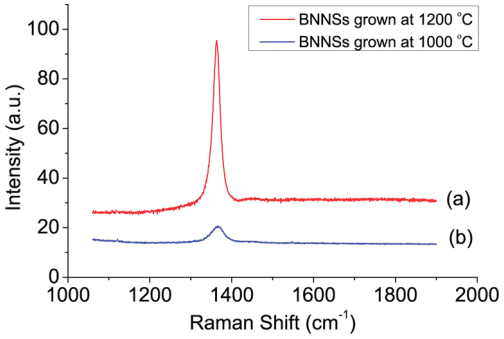

Figure 4. Raman spectra of (a) BNNSs synthesized at 1200 °C and (b) BNNSs synthesized at 1000 °C.

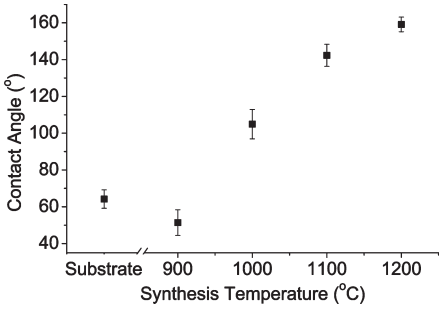

Figure 5. Water CAs measured on different BNNS coatings.

thicknesses are shown in Figure 3e after examining 50 sections in several TEM images; this exhibits that most of the BNNSs have thicknesses smaller than 4 nm. Figure 3b and c also indicate that the majority of BN layers are straight and parallel to each other; however, distorted layers and discontinuities exist as well. The chemical composition and stoichiometry of the synthesized BNNSs were further verified *via* electron energy loss spectroscopy (EELS). Figure 3f represents a typical EEL spectrum of the BNNSs having two distinct absorption features at 188 and 401 eV, indicating that only B and N K-shell ionization edges exist in the product. The sharp peaks on the left side of B−K and N−K edges correspond to 1s−π* antibonding orbits, and the peaks on the right side of the absorption edges correspond to 1s−σ* antibonding orbits. This type of EELS edge structure is typical of an sp^2-hybrizied layered BN. No trace of impurities is observed in the EEL spectrum, and quantification analysis gives a B/N atomic ratio of ~1.0.[51,52]

TEM characterization of the BNNSs synthesized at lower temperatures (*e.g.* 1000 °C) showed similar features to those synthesized at 1200 °C, suggesting that most of the BNNSs have thicknesses smaller than 5 nm. However, SAED patterns indicate that the BNNSs synthesized at 1000 °C consist of very fine grains, while the ones grown at higher temperatures are single crystals (see Supporting Information, Figure S1).

Raman spectroscopy was also used to characterize the BNNSs. Figure 4 shows typical Raman spectra of the BNNSs synthesized at 1000 and 1200 °C. The characteristic peaks seen at 1363 cm^{-1} in curve (a) and 1365 cm^{-1} in curve (b) are attributed to the B−N high-frequency vibrational mode (E_{2g}) within the h-BN layers, analogous to the G peak in graphene.[53] The reported Raman shift for different BN structures is in the range 1366−1374 cm^{-1}.[54−56]

It is stated that the position of high-frequency E_{2g} varies inversely with the crystallite size.[57] Also, a Raman peak frequency would shift to a higher frequency under a compressive stress and to a lower frequency under a tensile stress.[58] Very recently, it has been reported that the Raman peak is usually shifted upward and downward in monolayer and bilayer BN, respectively, compared with its position in bulk h-BN.[59] Monolayers show sample-dependent blue shifts of up to 4 cm^{-1} (*i.e.*, the Raman shift at ~1370 cm^{-1}), which is explained by a hardening of the E_{2g} phonon mode due to a slightly shorter B−N bond expected in the isolated monolayers.[59] The upshift of the Raman line to 1370 cm^{-1} has also been reported to be intrinsic for single-walled BN nanotubes (SW-BNNTs).[56] However, the TEM results revealed that the present BNNSs are multilayered; thus, they were expected to show the same features as bulk h-BN, *i.e.*, a Raman shift at 1366 cm^{-1}.[48] Nevertheless, the Raman spectra of our BNNSs show red shifts of 3 and 1 cm^{-1} for BNNSs synthesized at high and low temperatures, respectively. These red shifts can be due to the interactions of neighboring sheets in few-layered h-BN, leading to a small elongation of the B−N bond and consequently a softening of the phonons,[59] local temperature increase caused by the laser,[56] generation of stress in nanosheets due to the interactions with the substrate, and the intrinsic wrinkles of the BNNSs.[9] We speculate that the smaller red shift in curve (b) is attributed to the polycrystalline nature of the BNNSs grown at low temperature. Measurements of bulk polycrystalline h-BN specimens indicate that the Raman line is in the range 1367 to 1374 cm^{-1}.[57] However, we believe that in the case of our polycrystalline nanosheets the phonon softening due to stress and heating by the laser shifted the Raman peak down to 1365 cm^{-1} instead (for more discussion, see Supporting Information). Figure 4 also proves the absence of the carbon G band trace at ~1600 cm^{-1} in the Raman spectra and thus the high purity of the BNNSs synthesized by the present carbon-free CVD method.

Typical results of the X-ray energy dispersive spectroscopy (EDS) analysis and the corresponding elemental mappings over a large area indicated that the coatings were homogeneously composed of B and N species covering the Si/SiO_2 substrate (see Supporting Information, Figure S2). X-ray photoelectron spectroscopy (XPS) was also used to verify the chemical composition and purity of the BNNSs. The results showed typical sp^2 B−N bonding, implying that the coating

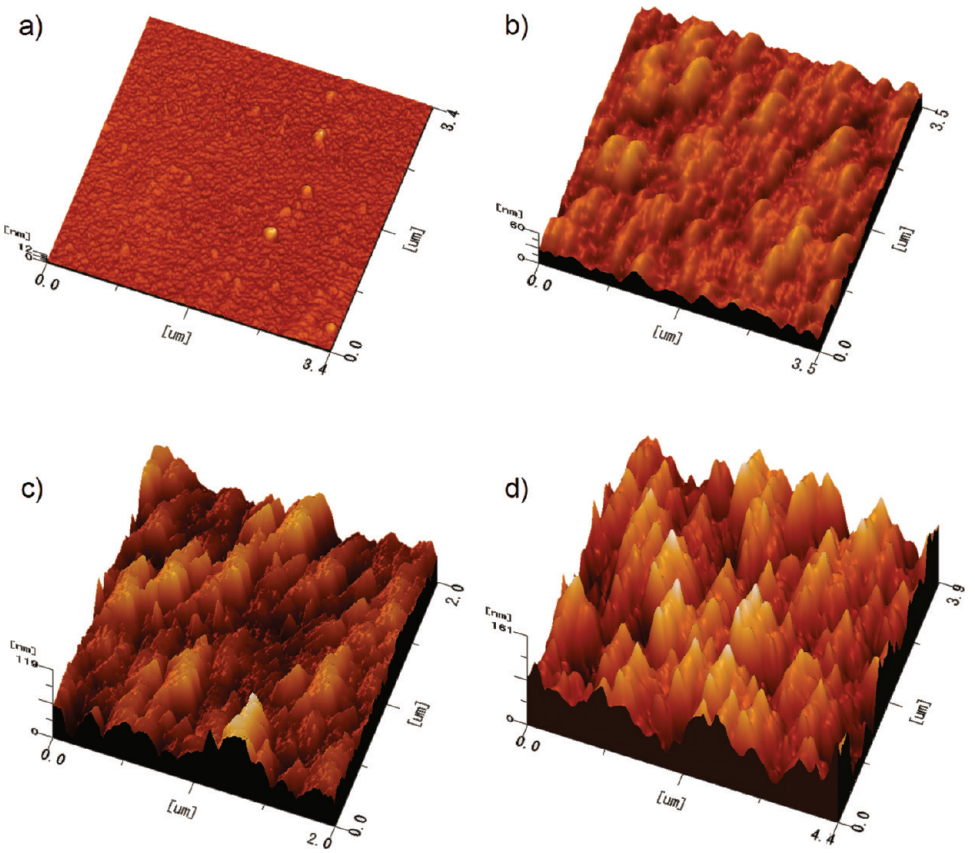

Figure 6. AFM topography images of BN coatings synthesized at (a) 900 °C, (b) 1000 °C, (c) 1100 °C, and (d) 1200 °C.

was made of hexagonal BN (see Supporting Information, Figure S3).

Water repellency of the BNNS coatings was investigated keeping in mind their special nanoscale features. Figure 5 shows the results of CA measurements conducted on pristine Si/SiO_2 wafers and the coatings grown at different temperatures for 30 min. The primary CA of a water droplet on the Si/SiO_2 wafer was 64.2°. This value decreased to 51.4° on the smooth BN coating grown at 900 °C, which is in agreement with the reported CA of granular BN films (48−55°)[35] and with our measurements on finely polished bulk BN plates (50−54°). The reason for this decline is the more hydrophilic nature of BN than the pristine substrate. However, by increasing the growth temperature from 900 to 1000 °C, the CA increased from 51.4° to 104.9°, revealing the transition from hydrophilicity to hydrophobicity. Further increase of the synthesis temperature to 1100 and 1200 °C resulted in enhanced hydrophobicity and superhydrophobicity of the coatings, with CAs reaching 142.3° and 159.1°, respectively.

Typical atomic force microscopy (AFM) images of the BNNSs are presented in Figure 6. Figure 6a represents the smooth surface of the coating grown at 900 °C corresponding to the observed hydrophilic behavior. Figure 6b, c, and d depict the topography of the coatings prepared at 1000, 1100, and 1200 °C, respectively. Quantitative analysis of the AFM images is also

TABLE 1. Topographical Properties of the BNNS Coatings

synthesis temperature (°C)	average roughness (R_a) (nm)	root mean square roughness (R_q) (nm)	maximum height difference (R_z) (nm)	surface roughness factor (S_r)
900	0.494	0.702	11.6	1.00
1000	7.46	9.33	60.2	1.02
1100	14.2	17.7	118.6	1.13
1200	23.4	28.7	161.1	1.15

shown in Table 1, verifying the escalation of the surface roughness by raising the synthesis temperature of the BNNSs (detailed definitions of the terms used in Table 1 are presented in the Supporting Information).

For a liquid droplet on an ideally flat film, the wettability is determined by the classical Young's equation:

$$\cos\theta_e = \frac{\gamma_{sv} - \gamma_{sl}}{\gamma_{lv}} \quad (1)$$

where θ_e is the contact angle in the Young's mode, γ is the surface tension, and subscript s, l, and v refer to the solid, liquid, and vapor phases, respectively. However, most of the solid surfaces are not truly flat; therefore, the surface roughness factor has to be considered during the evaluation of the surface wettability. This addition of surface texture can be explained by two independently developed models: the Wenzel

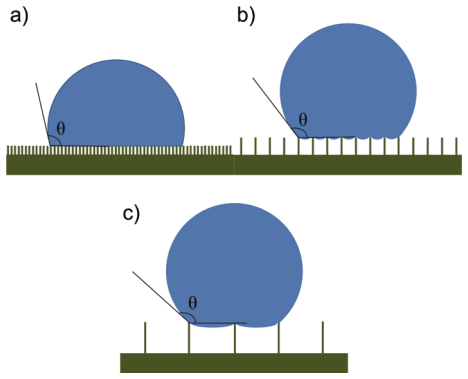

Figure 7. Schematic illustration of water CA on BNNS coatings prepared at (a) 1000 °C, (b) 1100 °C, and (c) 1200 °C in the frame of the Cassie–Baxter model.

model[60] given in eq 2 and the Cassie–Baxter model[61] given in eq 3:

$$\cos\theta_W = r\cos\theta_e \quad (2)$$

$$\cos\theta_{CB} = -1 + f_s(1+\cos\theta_e) \quad (3)$$

where r is the surface roughness (*i.e.*, the ratio of total surface area to the projected area on the horizontal plane) and f_s is the fraction of solid–liquid contact. In Wenzel's formulation, it is assumed that the liquid fills up the rough surface, therefore increasing the interfacial contact area of the solid and the liquid. But in Cassie's model, the liquid is assumed to form a line of contact on the rough surface with air trapped below the contact line. In our system, θ_e could be equal to ~51.4°, because the surface roughness factor for the smooth BNNS coatings grown at 900 °C is 1.00, giving $\theta_W = \theta_e = 51.4°$ in eq 2. Wenzel's formulation predicts that when $\theta_e > 90°$, the effect of increasing roughness is to further increase θ_W toward 180°; however, when $\theta_e < 90°$, the effect of increasing roughness is to further reduce θ_W toward 0°. That is contradictory to our measurements, since increasing the surface roughness of the BNNS coatings enhances the water CA from 51.4° to 159.1°, showing an alterable behavior of the coatings from hydrophilicity to superhydrophobicity. While Wenzel's model predicts an opposite trend, that is, considering the surface roughness factors of 1.00 and 1.15 for the BNNSs grown at 1000 and 1200 °C, respectively, Wenzel's equation suggests that the CA decreases from 51.4° to 44.2° by increasing the surface roughness. Therefore, we adopt Cassie–Baxter formula for our system supposing that the liquid bridges the surface features and does not penetrate between the spaces separating them. Equation 3 predicts the fractions of solid–liquid contact to be 0.46, 0.13, and 0.04 for the BNNS coatings grown at 1000, 1100, and 1200 °C, respectively. A schematic representation of water droplets on the BNNS coatings is illustrated in Figure 7. It is assumed that the liquid contacts only the flat parts

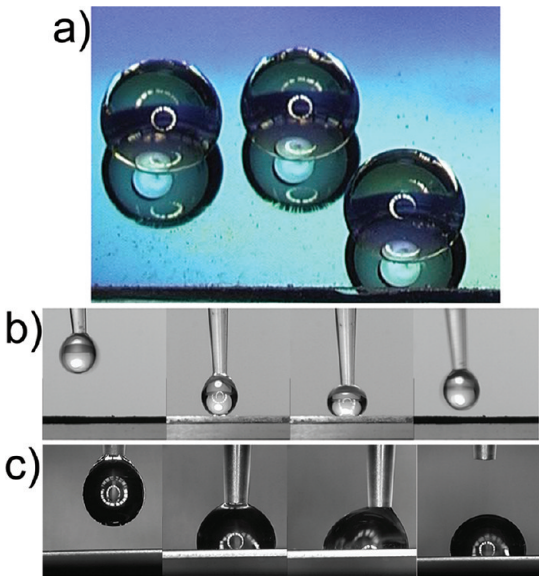

Figure 8. Typical photograph showing water droplets on the BNNS coating synthesized at 1200 °C (a). Images showing the approach and withdrawal of a water droplet from the BNNS coating synthesized at 1200 °C (b) and 1000 °C (c).

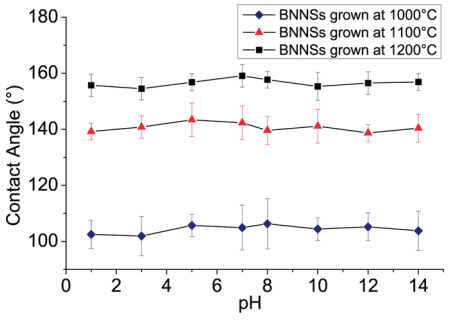

Figure 9. Effect of droplet pH variations on the CA of BNNSs grown at different temperatures.

of the surface and the menisci below the droplet are due to the liquid's weight. These illustrations are in good agreement with the height profile analysis of the present BNNS coatings prepared at different temperatures (see Figure S4 in Supporting Information). Although the roughness factor (r) is not present in the Cassie–Baxter formula, it is indirectly considered in determination of the balance between f_s and r for the threshold CA at which the Wenzel state changes into the Cassie–Baxter state, as discussed by Bico *et al.*[62]

Using the calculated f_s values, we can conclude that the trapped air within the nanostructures plays an important role in promoting superhydrophobicity in the BNNS coatings. In other words, by raising the synthesis temperature the fraction of solid decreases and the fraction of air (f_v) in the composite interface increases. This enhancement of f_v and the increase of roughness are the major causes to create superhydrophobicity in the present BNNS coatings (the importance of surface roughness in characterizing the

wetting properties of the BNNS coatings was further verified by a simple test; see Supporting Information, Figure S5). It should be noted that the lack of liquid penetration in the separation space between the droplet and the substrate may not be only due to an inability of air to escape. Whether a liquid will penetrate into the rough structure or not can also be determined by the cost in surface free energy for wetting down the surface structure.[63]

Figure 8a shows a photograph of spherical water droplets on a BNNS coating prepared at 1200 °C, indicating its nonwetting nature. In order to further investigate the nonwetting properties, a suspended water droplet was moved toward a BNNS coating prepared at 1200 °C (Figure 8b). Then the droplet was pushed against the coating, and finally the droplet was withdrawn from the coating surface. No visual water residue was left on the coating, indicating that the adhesion force between the BNNS coating and the droplet is much weaker than that between the droplet and the needle. The same experiment was carried out on a BNNS coating prepared at 1000 °C, as depicted in Figure 8c. However, for this less hydrophobic coating the water droplet adhered to the coating and was detached from the syringe during withdrawal. This experiment also indicates that the BNNS coatings synthesized at 1200 °C have superior nonwetting properties to those synthesized at lower temperatures.

Moreover, the BNNS coatings showed stable hydrophobic properties over a wide range of pH, from 1 to 14, as shown in Figure 9. Because of the outstanding chemical inertness of the BNNSs, even strongly acidic and basic conditions do not affect their nonwetting properties. The same behavior has been reported for the BNNT films,[35,64] suggesting that the superhydrophobic BN nanostructures can be excellent candidates for self-cleaning applications.

Finally, self-cleaning tests on the BNNS coatings revealed that the coatings synthesized at 1200 °C are more efficient than those synthesized at 1000 °C (see Supporting Information, Figure S6). The adhesion between the particle and the BNNS coating can be attributed to f_s,[65] assuming that a lower contact area between the particles and the surfaces is achieved as f_s decreases. In coatings prepared at higher temperatures, a small contact area decreases the adhesion of the particle to the surface and leads to a more efficient self-cleaning coating.

CONCLUSION

In summary, we performed a systematic study on the synthetic parameters and structural features of BNNS coatings on Si/SiO_2 substrates made through a simple and facile procedure in a conventional horizontal tube furnace. The majority of the obtained BNNSs were less than 5 nm in thickness, and their purity was confirmed by several characterization techniques including EDS, EELS, XPS, and Raman spectroscopy. The morphology, roughness, and water-repelling properties of the coatings were successfully controlled by the process variables. As a result, a wide range of water CAs, from ~51° to ~159°, were obtained, indicating a significant change from hydrophilicity to superhydrophobicity of the coatings. The wetting characteristics of the coatings were independent of the water pH value and were explained in detail by the Cassie–Baxter model. Considering the chemical inertness and the stability of the BNNSs in a broad range of temperatures, we anticipate future industrial applications for the BNNSs as superhydrophobic self-cleaning coatings.

METHODS

The crystalline BNNSs were grown in a horizontal electric furnace consisting of a fused quartz tube 100 cm in length and 10 cm in diameter, as shown in Figure 1. Initially, B, MgO, and FeO powders were mechanically mixed at the molar ratio of 2:1:1. In each experiment a total of 500 mg of the mixed powders was used as the precursor, positioned in an alumina combustion boat covered by a commercially available Si/SiO_2 substrate. The boat was then placed inside a quartz test tube, near the closed end, and the test tube was set into the horizontal quartz vacuum chamber so the closed end was located at the center of the heating zone. The quartz tube chamber was evacuated to ~1 Torr, and subsequently ammonia gas was flowed into the chamber at the rate of 0.4 mL/min. Then, the precursors were heated to 900–1200 °C, held for 30–60 min, and cooled to room temperature. The chemical compositions and morphologies of the products were characterized using an X-ray energy dispersive spectrometer attached to a thermal field emission scanning electron microscope (FE-SEM; Hitachi SU8000). X-ray photoelecton spectroscopy was also performed using monochromatic aluminum KR X-rays to further characterize the chemical composition of the coatings. The Avantage software was used for XPS data analyses. The structures of the BNNSs were studied by a high-resolution field emission transmission electron microscope (JEOL, JEM-2100F) equipped with an electron energy loss spectrometer. Raman spectroscopy was performed by means of a LabRam HR-800 Raman microscope (Horiba, Japan) at 514.5 nm laser excitation. Topographical images of the coatings were obtained by a JEOL JSPM-5200 scanning probe microscope using silicon cantilevers NSC36-C (Micromash Inc., tip radius <10 nm) in the tapping atomic force microscopy mode at ambient conditions. The contact angle measurements were carried out by a sessile drop method. A deionized water droplet of about 10 μL volume was positioned on the coating by a microsyringe. A high-resolution Keyence VH-5000 optical instrument equipped with WinROOF V5.03 analysis software was used for measuring the CA of water droplets. Each CA value and its standard deviation were the results of at least 10 measurements carried out in ambient environment, at room temperature (~24 °C) and a relative humidity of ~40%. In order to investigate the effect of pH on superhydrophobicity of the BNNS coatings, either diluted NaOH or HCl was used to adjust the pH value of the liquid.

For self-cleaning tests, MgO particles (<10 μm) were dispersed on the BNNS coatings followed by placement of water droplets on them. The self-cleaning efficiency of the BNNS coatings was then determined by water droplets rolling off under 5−15° tilting of the substrates.

Acknowledgment. This project was supported by the National Institute for Materials Science (NIMS; Tsukuba, Japan). This work was performed in the World Premier International Center for Materials Nanoarchitectonics (MANA). The authors are grateful to Dr. Yoshihiro Nemoto for his assistance with HRTEM.

Supporting Information Available: Chemical composition analysis by EDS and XPS, TEM images and EEL spectrum of the BNNS coatings prepared at 1000 °C, more discussion on Raman spectroscopy results, typical AFM images of the BNNS coatings prepared at 1000 and 1200 °C and their height profile analysis, morphology-related CA test results, self-cleaning efficiency test results, and detailed definitions of surface roughness parameters mentioned in Table 1 of the main text. This material is available free of charge *via* the Internet at http://pubs.acs.org.

REFERENCES AND NOTES

1. Frank, I. W.; Tanenbaum, D. M.; van der Zande, A. M.; McEuen, P. L. Mechanical Properties of Suspended Graphene Sheets. *J. Vac. Sci. Technol. B* **2007**, *25*, 2558–2561.
2. Shang, N. G.; Papakonstantinou, P.; McMullan, M.; Chu, M.; Stamboulis, A.; Potenza, A.; Dhesi, S. S.; Marchetto, H. Catalyst-Free Efficient Growth, Orientation and Biosensing Properties of Multilayer Graphene Nanoflake Films with Sharp Edge Planes. *Adv. Funct. Mater.* **2008**, *18*, 3506–3514.
3. Bolotin, K. I.; Sikes, K. J.; Jiang, Z.; Klima, M.; Fudenberg, G.; Hone, J.; Kim, P.; Stormer, H. L. Ultrahigh Electron Mobility in Suspended Graphene. *Solid State Commun.* **2008**, *146*, 351–355.
4. Zhao, X.; Tian, H.; Zhu, M. Y.; Tian, K.; Wang, J. J.; Kang, F. Y.; Outlaw, R. A. Carbon Nanosheets as the Electrode Material in Supercapacitors. *J. Power Sources* **2009**, *194*, 1208–1212.
5. Stoller, M. D.; Park, S.; Zhu, Y.; An, J.; Ruoff, R. S. Graphene-Based Ultracapacitors. *Nano Lett.* **2008**, *8*, 3498–3502.
6. Yu, A. P.; Ramesh, P.; Sun, X. B.; Bekyarova, E.; Itkis, M. E.; Haddon, R. C. Enhanced Thermal Conductivity in a Hybrid Graphite Nanoplatelet-Carbon Nanotube Filler for Epoxy Composites. *Adv. Mater.* **2008**, *20*, 4740–4744.
7. Patchkovskii, S.; Tse, J. S.; Yurchenko, S. N.; Zhechkov, L.; Heine, T.; Seifert, G. Graphene Nanostructures as Tunable Storage Media for Molecular Hydrogen. *Proc. Natl. Acad. Sci. U. S. A.* **2005**, *102*, 10439–10444.
8. Schedin, F.; Geim, A. K.; Morozov, S. V.; Hill, E. W.; Blake, P.; Katsnelson, M. I.; Novoselov, K. S. Detection of Individual Gas Molecules Adsorbed on Graphene. *Nat. Mater.* **2007**, *6*, 652–655.
9. Song, L.; Ci, L. J.; Lu, H.; Sorokin, P. B.; Jin, C. H.; Ni, J.; Kvashnin, A. G.; Kvashnin, D. G.; Lou, J. Yakobson, B. I.; *et al*. Large Scale Growth and Characterization of Atomic Hexagonal Boron Nitride Layers. *Nano Lett.* **2010**, *10*, 3209–3215.
10. Lin, Y.; Williams, T. V.; Connell, J. W. Soluble, Exfoliated Hexagonal Boron Nitride Nanosheets. *J. Phys. Chem. Lett.* **2010**, *1*, 277–283.
11. Zeng, H.; Zhi, C. Y.; Zhang, Z.; Wei, X.; Wang, X.; Guo, W.; Bando, Y.; Golberg, D. "White Graphenes": Boron Nitride Nanoribbons *via* Boron Nitride Nanotube Unwrapping. *Nano Lett.* **2010**, *10*, 5049–5055.
12. Han, W. Q.; Wu, L. J.; Zhu, Y. M.; Watanabe, K.; Taniguchi, T. Structure of Chemically Derived Mono- and Few-Atomic-Layer Boron Nitride Sheets. *Appl. Phys. Lett.* **2008**, *93*, 223103-1–223103-3.
13. Mohai, I.; Mohai, M; Bertóti, I.; Sebestyén, Z.; Németh, P.; Babievskaya, I. Z.; Szépvölgyi, J. Formation of Thin Boron Nitride Coating on Multiwall Carbon Nanotube Surfaces. *Diam. Relat. Mater.* **2011**, *20*, 227–231.
14. Li, J. S.; Zhang, C. R.; Li, B. Preparation and Characterization of Boron Nitride Coatings on Carbon Fibers from Borazine by Chemical Vapor Deposition. *Appl. Surf. Sci.* **2011**, *257*, 7752–7757.
15. Wang, W. L.; Bi, J. Q.; Sun, W. X.; Zhu, H. L.; Xu, J. J.; Zhao, M. T.; Bai, Y. J. Facile Synthesis of Boron Nitride Coating on Carbon Nanotubes. *Mater. Chem. Phys.* **2010**, *122*, 129–132.
16. Gomathi, A.; Ramya Harika, M.; Rao, C. N. R. Urea Route to Coat Inorganic Nanowires, Carbon Fibers and Nanotubes by Boron Nitride. *Mater. Sci. Eng., A* **2008**, *476*, 29–33.
17. Chen, L.; Ye, H.; Gogotsi, Y. Carbothermal Synthesis of Boron Nitride Coatings on Silicon Carbide. *J. Am. Ceram. Soc.* **2003**, *86*, 1830–1837.
18. Chen, L.; Ye, H.; Gogotsi, Y. Synthesis of Boron Nitride Coating on Carbon Nanotubes. *J. Am. Ceram. Soc.* **2004**, *87*, 147–151.
19. Li, G. X.; Liu, Y.; Wang, B.; Song, X. M.; Li, E.; Yan, H. Preparation of Transparent BN Films with Superhydrophobic Surface. *Appl. Surf. Sci.* **2008**, *254*, 5299–5303.
20. Feng, L.; Li, S. H.; Li, Y. S.; Li, H. J.; Zhang, L. J.; Zhai, J.; Song, Y. L.; Liu, B. Q.; Jiang, L.; Zhu, D. B. Super-Hydrophobic Surfaces: From Natural to Artificial. *Adv. Mater.* **2002**, *14*, 1857–1860.
21. Steele, A.; Bayer, I.; Moran, S.; Cannon, A.; King, W. P.; Loth, E. Conformal ZnO Nanocomposite Coatings on Micro-Patterned Surfaces for Superhydrophobicity. *Thin Solid Films* **2010**, *518*, 5426–5431.
22. Han, J. T.; Xu, X.; Cho, K. Diverse Access to Artificial Superhydrophobic Surfaces Using Block Copolymers. *Langmuir* **2005**, *21*, 6662–6665.
23. Öner, D.; McCarthy, T. J. Ultrahydrophobic Surfaces. Effects of Topography Length Scales on Wettability. *Langmuir* **2000**, *16*, 7777–7782.
24. Barthlott, W.; Neinhuis, C. Purity of the Sacred Lotus, or Escape from Contamination in Biological Surfaces. *Planta* **1997**, *202*, 1–8.
25. Morra, M.; Occhiello, E.; Garbassi, F. Contact Angle Hysteresis in Oxygen Plasma Treated Poly(tetrafluoroethylene). *Langmuir* **1989**, *5*, 872–876.
26. Zhang, X.; Shi, F.; Yu, X.; Liu, H.; Fu, Y.; Wang, Z.; Jiang, L.; Li, X. Polyelectrolyte Multilayer as Matrix for Electrochemical Deposition of Gold Clusters: Toward Super-Hydrophobic Surface. *J. Am. Chem. Soc.* **2004**, *126*, 3064–3065.
27. Tsujii, K.; Yamamoto, T.; Onda, T.; Shibuchi, S. Super Oil-Repellent Surfaces. *Angew. Chem., Int. Ed.* **1997**, *36*, 1011–1012.
28. Li, H.; Wang, X.; Song, Y.; Liu, Y.; Li, Q.; Jiang, L.; Zhu, D. Super-"Amphiphobic" Aligned Carbon Nanotube Films. *Angew. Chem., Int. Ed.* **2001**, *113*, 1793–1796.
29. Feng, X.; Feng, L.; Jin, M.; Zhai, J.; Jiang, L.; Zhu, D. Reversible Super-Hydrophobicity to Super-Hydrophilicity Transition of Aligned ZnO Nanorod Films. *J. Am. Chem. Soc.* **2004**, *126*, 62–63.
30. Feng, X.; Zhai, J.; Jiang, L. The Fabrication and Switchable Superhydrophobicity of TiO_2 Nanorod Films. *Angew. Chem., Int. Ed.* **2005**, *44*, 5115–5118.
31. Lai, Y.; Lin, C.; Wang, H.; Huang, J.; Zhuang, H.; Sun, L. Superhydrophilic-Superhydrophobic Micropattern on TiO_2 Nanotube Films by Photocatalytic Lithography. *Electrochem. Commun.* **2008**, *10*, 387–391.
32. Zhao, Y. S.; Yang, W.; Zhang, G.; Ma, Y.; Yao, J. A Hierarchical Self-Assembly of 4,5-Diphenylimidazole on Copper. *Colloids Surf. A: Physicochem. Eng. Aspects* **2006**, *277*, 111–118.
33. Li, X.; Tay, B. K.; Miele, P.; Brioude, A.; Cornu, D. Fabrication of Silicon Pyramid/Nanowire Binary Structure with Superhydrophobicity. *Appl. Surf. Sci.* **2009**, *255*, 7147–7152.
34. Shiu, J. Y.; Kuo, C. W.; Chen, P.; Mou, C. Y. Fabrication of Tunable Superhydrophobic Surfaces by Nanosphere Lithography. *Chem. Mater.* **2004**, *16*, 561–564.
35. Lee, C. H.; Drelich, J.; Yap, Y. K. Superhydrophobicity of Boron Nitride Nanotubes Grown on Silicon Substrates. *Langmuir* **2009**, *25*, 4853–4860.

36. Shang, H. M.; Wang, Y.; Limmer, S. J.; Chou, T. P.; Cao, G. Z. Optically Transparent Superhydrophobic Silica-Based Films. *Thin Solid Films* **2005**, *472*, 37–43.
37. Guo, Z.; Zhou, F.; Hao, J.; Liu, W. Stable Biomimetic Super-Hydrophobic Engineering Materials. *J. Am. Chem. Soc.* **2005**, *127*, 15670–15671.
38. Xu, Y.; Wu, D.; Sun, Y. H.; Huang, Z. X.; Jiang, X. D.; Wei, X. F.; Wei, Z. H.; Dong, B. Z.; Wu, Z. H. Superhydrophobic Antireflective Silica Films: Fractal Surfaces and Laser-Induced Damage Thresholds. *Appl. Opt.* **2005**, *44*, 527–533.
39. Li, M.; Zhai, J.; Liu, H.; Song, Y. L.; Jiang, L.; Zhu, D. B. Electrochemical Deposition of Conductive Superhydrophobic Zinc Oxide Thin Films. *J. Phys. Chem. B* **2003**, *107*, 9954–9957.
40. Lee, J.; Kim, C. J. Surface-Tension-Driven Microactuation Based on Continuous Electrowetting. *Microelectromech. Syst.* **2000**, *9*, 171–180.
41. Verplanck, N.; Galopin, E; Camart, J. C.; Thomy, V.; Coffinier, Y.; Boukherroub, R. Reversible Electrowetting on Superhydrophobic Silicon Nanowires. *Nano Lett.* **2007**, *7*, 813–817.
42. Hayes, R. A.; Feenstra, B. J. Video-Speed Electronic Paper Based on Electrowetting. *Nature* **2003**, *425*, 383–385.
43. Lee, C. H.; Wang, J.; Kayatsha, V. K.; Huang, J. Y.; Yap, Y. K. Effective Growth of Boron Nitride Nanotubes by Thermal Chemical Vapor Deposition. *Nanotechnology* **2008**, *19*, 455605-1–455605-5.
44. Wu, Y.; Qiao, P.; Chong, T.; Shen., Z. Carbon Nanowalls Grown by Microwave Plasma Enhanced Chemical Vapor Deposition. *Adv. Mater.* **2002**, *14*, 64–67.
45. Zhu, M. Y.; Wang, J. J.; Holloway, B. C.; Outlaw, R. A.; Zhao, X.; Hou, K.; Shutthanandan, V.; Manos, D. M. A Mechanism for Carbon Nanosheet Formation. *Carbon* **2007**, *45*, 2229–2234.
46. Mensah, S. L.; Kayastha, V. K.; Ivanov, I. N.; Geohegan, D. B.; Yap, Y. K. Formation of Single Crystalline ZnO Nanotubes without Catalysts and Templates. *Appl. Phys. Lett.* **2007**, *90*, 113108-1–113108-3.
47. Blakely, J. M.; Jackson, K. A. Growth of Crystal Whiskers. *J. Chem. Phys.* **1962**, *37*, 428–430.
48. Yu, J.; Qin, L.; Hao, Y.; Kuang, S.; Bai, X. D.; Chong, Y. M.; Zhang, W.; Wang., E. G. Vertically Aligned Boron Nitride Nanosheets: Chemical Vapor Synthesis, Ultraviolet Light Emission, and Superhydrophobicity. *ACS Nano* **2010**, *4*, 414–442.
49. Zhi, C. Y.; Bando, Y.; Tang, C. C.; Kuwahara, H.; Golberg, D. Large-Scale Fabrication of Boron Nitride Nanosheets and Their Utilization in Polymeric Composites with Improved Thermal and Mechanical Properties. *Adv. Mater.* **2009**, *21*, 2889–2893.
50. Regan, W.; Alem, N.; Aleman, B.; Geng, B.; Girit, C.; Maserati, L.; Wang, F.; Crommie, M.; Zettl, A. A Direct Transfer of Layer-Area Graphene. *Appl. Phys. Lett.* **2010**, *96*, 113102-1–113102-3.
51. Yin, L. W.; Bando, Y.; Golberg, D.; Gloter, A.; Li, M. S.; Yuan, X. L.; Sekiguchi, T. Porous BCN Nanotubular Fibers: Growth and Spatially Resolved Cathodoluminescence. *J. Am. Chem. Soc.* **2005**, *126*, 16354–16355.
52. Chen, Z. G.; Li, F.; Wang, Y.; Wang, L. Z.; Yuan, X. L.; Sekiguchi, T.; Cheng, H. M.; Lu, G. Q. Novel Boron Nitride Hollow Nanoribbons. *ACS Nano* **2008**, *2*, 2183–2191.
53. Wu, J.; Han, W. Q.; Walukiewicz, W.; Ager III, J. W.; Shan, W.; Haller, E. E.; Zettl, A. Raman Spectroscopy and Time-Resolved Photoluminescence of BN and $B_xC_yN_z$ Nanotubes. *Nano Lett.* **2004**, *4*, 647–650.
54. Hoffman, D. M.; Doll, G. L.; Eklund, P. C. Optical Properties of Pyrolytic Boron Nitride in the Energy Range 0.05−10 eV. *Phys. Rev. B* **1984**, *30*, 6051–6056.
55. Geick, R.; Perry, C. H.; Rupprecht, G. Normal Modes in Hexagonal Boron Nitride. *Phys. Rev.* **1966**, *146*, 543–547.
56. Arenal, R.; Ferrari, A. C.; Reich, S.; Wirtz, L.; Mevellec, J. Y.; Lefrant, S.; Rubio, A.; Loiseau, A. Raman Spectroscopy of Single-Wall Boron Nitride Nanotubes. *Nano Lett.* **2006**, *6*, 1812–1816.
57. Nemanich, R. J.; Solin, S. A.; Martin, R. M. Light-Scattering Study of Boron-Nitride Micro-Crystals. *Phys. Rev. B* **1981**, *23*, 6348–6356.
58. Kuzuba, T.; Sato, Y.; Yamaoka, S.; Era, K. Raman-Scattering Study of High-Pressure Effects on the Anisotropy of Force Constants of Hexagonal Boron Nitride. *Phys. Rev. B* **1978**, *18*, 4440–4443.
59. Gorbachev, R. V.; Riaz, I.; Nair, R. R.; Jalil, R.; Britnell, L.; Belle, B. D.; Hill, E. W.; Novoselov, K. S.; Watanabe, K.; Taniguchi, T.; *et al*. Hunting for Monolayer Boron Nitride: Optical and Raman Signatures. *Small* **2011**, *7*, 465–468.
60. Wenzel, R. N. Resistance of Solid Surfaces to Wetting by Water. *Ind. Eng. Chem.* **1936**, *28*, 988–994.
61. Cassie, A. B. D.; Baxter, S. Wettability of Porous Surfaces. *Trans. Faraday Soc.* **1944**, *40*, 546–551.
62. Bico, J.; Thiele, U.; Quere, D. Wetting of Textured Surfaces. *Colloids Surf. A: Physicochem. Eng. Aspects* **2002**, *206*, 41–46.
63. Shirtcliffe, N. J.; McHale, G.; Artherton, S.; Newton, M. I. An Introduction to Superhydrophobicity. *Adv. Colloid Interface Sci.* **2010**, *161*, 124–138.
64. Li, L. H.; Chen, Y. Superhydrophobic Properties of Non-aligned Boron Nitride Nanotube Films. *Langmuir* **2010**, *26*, 5135–5140.
65. Bhushan, B.; Jung, Y. C.; Koch, K. Self-Cleaning Efficiency of Artificial Superhydrophobic Surfaces. *Langmuir* **2009**, *25*, 3240–3248.